Catalysis Science & Technology

Higher Loadings of Pt Single-Atom and Clusters over Reducible Metal Oxides: Application to C-O Bond Activation

Journal:	*Catalysis Science & Technology*
Manuscript ID	CY-ART-01-2022-000193.R1
Article Type:	Paper
Date Submitted by the Author:	09-Mar-2022
Complete List of Authors:	Wang, Yunzhu; University of Delaware, Catalysis Center for Energy Innovation Lee, Seungyeon; University of Delaware, Catalysis Center for Energy Innovation; University of Delaware, Department of Chemical and Biomolecular Engineering Zhou, Jiahua; University of Delaware, Catalysis Center for Energy Innovation; University of Delaware, Department of Chemical and Biomolecular Engineering Fu, Jiayi; University of Delaware, Catalysis Center for Energy Innovation; University of Delaware, Catalysis Center for Energy Innovation Foucher, Alexandre; University of Pennsylvania, Material Science Stach, Eric; University of Pennsylvania, Materials Science and Engineering Ma, Lu; Brookhaven National Laboratory, National Synchrotron Light Source II Marinkovic, Nebojsa; Brookhaven National Laboratory, National Synchrotron Light Source II Ehrlich, Steven; Brookhaven National Laboratory, National Synchrotron Light Source II Zheng, Weiqing; University of Delaware, Catalysis Center for Energy Innovation Vlachos, Dion; University of Delaware, Catalysis Center for Energy Innovation; University of Delaware, Department of Chemical and Biomolecular Engineering

Higher Loadings of Pt Single-Atom and Clusters over Reducible Metal Oxides: Application to C-O Bond Activation

Yunzhu Wang,[1] Seungyeon Lee,[1,2] Jiahua Zhou,[1,2] Jiayi Fu,[1,2] Alexandre Foucher,[3] Eric Stach,[3] Lu Ma,[4] Nebojsa Marinkovic,[4] Steven Ehrlich,[4] Weiqing Zheng,[1]* Dionisios G. Vlachos[1,2]*

1. Catalysis Center for Energy Innovation, University of Delaware, Newark, DE 19716, USA
2. Department of Chemical and Biomolecular Engineering, University of Delaware, Newark, DE 19716, USA
3. Department of Chemical and Biomolecular Engineering, University of Pennsylvania, Philadelphia, PA 19104, USA
4. National Synchrotron Light Source II, Brookhaven National Laboratory, Upton, NY 11973, USA

*Corresponding authors: Weiqing Zheng weiqing@udel.edu; Dionisios G. Vlachos vlachos@udel.edu

Abstract

We develop higher loading of isolated noble metal atoms and clusters on a mildly reducible metal oxide. We demonstrated the approach for Pt supported on TiO_2 and confirmed it by XRD, AC-HAADF-STEM, CO-FTIR, XAS, and XPS. Density functional theory calculations rationalize the experimental stability and the IR shifts by mixtures of CH_3I and CO. The redispersed catalysts are thermally stable in inert gas or H_2 and afford enhanced selectivity and activity in hydrodeoxygenation reactions than metal nanoparticles by creating surface oxygen vacancies that promote C-O cleavage without side reactions. Higher metal loadings, e.g., 1%Pt/TiO_2, on the oxide surface profoundly increase the activity of the bare oxide catalyst and tenfold compared to ultra-low loadings typically used for single atom catalysis.

Keywords: redispersion; single-atoms catalysts; hydrodeoxygenation; metal oxides

1. Introduction

C-O bond scission is crucial in many reactions, such as Fisher Tropsch, biomass conversion, and CO_2 upgrade. Specifically, hydrodeoxygenation (HDO) is ubiquitous in biomass conversion for decreasing its oxygen content.[1-4] Transition metals are typically active for HDO but not selective. They interact strongly with unsaturated rings to induce hydrogenolysis and hydrogenation of unsaturated C=C and C=O bonds.[5-7] Our group has found that the redox sites of reducible metal oxides enable HDO reactions of the side groups of furans without ring-hydrogenation and ring-opening.[8] The rate depends on the catalyst's ability to form oxygen vacancies while remaining stable under reaction conditions. This trade-off gives rise to a volcano curve dictated by activity and stability. Highly reducible metal oxides, such as RuO_x and IrO_x, are at the top of the volcano and afford a high HDO rate but are reduced during the reaction. Doping noble metal single-atom catalysts (SACs) on relatively stable metal oxides, such as titania oxide (TiO_2), enhances the HDO activity by forming surface oxygen vacancies.[9] For example, 0.04 wt% Pt loading on TiO_2 increases the HDO rate 30 times over pristine TiO_2. A 25x increase in Pt loading to 1 wt% would enhance the rate proportionally. However, the strong electrostatic adsorption (SEA) method, used previously, leads to nanoparticles (NPs) for higher Pt loadings. The NPs are less active for HDO and cause side reactions by adsorbing the rings strongly.[10]

SACs have attracted increasing attention due to their often superior catalytic efficiency, better metal atom utilization, and intense interaction with the support.[11-13] Several methods have been exploited for their synthesis.[14-20] Most synthesis methods focus on low-loadings to avoid sintering stemming from their intrinsic thermal instability.[21-24] Redispersion of metal NPs to increase metal dispersion and atom efficiency has been investigated for years.[25] It was recently demonstrated that supported NPs could be redispersed to atoms or small clusters[19, 25-28] using iodomethane (CH_3I) and CO at low temperatures. The method was developed for carbon-supported Au NPs to produce clusters of 2-3 atoms under CH_3I and H_2/CO at 240 °C and 16 bar.[29] Bromomethane (CH_3Br) is also effective.[30, 31] Ru, Rh, Pd, Ag, Ir, and Pt NPs on carbon were also dispersed.[32-34] The iodine radical and CO break the metal-metal bonds, forming mononuclear complexes stabilized by the oxygen-containing functional groups of the carbon support.[32] This method was extended to Au NPs supported on γ-Al_2O_3 and TiO_2, giving rise to NPs (~2.0 nm), clusters, and atoms.[35] Pt NPs have been redispersed on activated carbon (AC) but not on reducible metal oxides, e.g., TiO_2. Furthermore, their application in complex chemistry, such as the HDO reaction, has not been demonstrated either. HDO chemistry is an ideal probe to test the effectiveness of the redispersion.

Herein, we demonstrate the redispersion of Pt NPs to SACs on TiO_2 through CH_3I/CO treatment. Extensive characterization confirms isolated Pt atoms and well-dispersed sub-nanoclusters. Density functional theory (DFT) calculations rationalize the IR shifts and stability of small Pt clusters. The redispersed catalysts were stable upon thermal treatment in inert gas or H_2. They exposed better selectivity and enhanced activity in HDO than Pt NPs with the same metal loading, suggesting a synergistic effect of a high density of redox sites and abundant surface oxygen vacancies.

2. Methods

Catalyst Preparation

1 wt% and 2 wt% Pt/TiO_2 were prepared by the incipient wetness impregnation (IWI) method. Tetraammineplatinum(II) nitrate ($[Pt(NH_3)_4](NO_3)_2$, Alfa Aesar) was dissolved in 50/50 (v/v) methanol/water precursor solution. The solution was added to anatase TiO_2 powder (5 nm nanoparticles from the US Research Nanomaterials, Stock #: US3838) with vigorous stirring to form a paste. The paste

was dried at 90 °C overnight and calcined in 200 ml/min air at 450 °C for 4 h at 10 °C/min to remove NH_3 and NO_3^-. The calcined Pt/TiO_2 sample was reduced in 200 ml/min 10% H_2/Ar at 250 °C for 4 h at 2 °C/min. Hereafter, x in xPt_{NP} represents the weight percent of supported Pt NPs.

For redispersion, upon reduction, the sample was cooled down to room temperature and the gas was switched to 100 ml/min Ar. The sample was then heated to 240 °C and held for 20 min. 30 ml/min CO then passed through liquid CH_3I (Sigma Aldrich) and treated the sample at 240 °C for 6 h. The sample was cooled to room temperature under 100 ml/min Ar. The redispersed sample was labeled as xPt_1. The $1Pt_1$ was post-treated under 100 ml/min 10% H_2/Ar or Ar at 250 °C for 2 h at 2 °C/min. The catalysts were labeled as $1Pt_1$-H_2 and $1Pt_1$-Ar, respectively.

Catalyst Characterization

Fourier-transform infrared (FTIR) of CO adsorption was conducted at 25 °C. The catalyst sample was pressed into a thin pellet (< 0.3 mm thickness) and held in a customized *in-situ* cell. The pellet was reduced in a 100 ml/min flowing 10% H_2/Ar stream at 250°C for 1 h and kept at 250 °C in a vacuum for 1 h. After cooling down to 25 °C in a vacuum, the background spectrum was collected. Multiple CO doses were carried out at 25 °C until full saturation.

Aberration-corrected high-angle-annular-dark-field scanning transmission electron microscopy (AC-HAADF-STEM) images were obtained using a JEOL NEOARM operated at 200 kV and equipped with a probe aberration corrector (spatial resolution ~0.63 Å). The conversion angle for HAADF-STEM imaging is measured as 22 mrad, and its collection angle is 64-342 mrad. The contrast of the images is proportional to the atomic number of the sample (Z-contrast). All samples were prepared by depositing a drop of diluted sample on lacy-carbon coated copper grids.

Powder X-ray diffraction (XRD) measurements were carried out on a Bruker D8 diffractometer using a Cu Kα source (λ = 1.5418 Å). Wavelength dispersive X-ray fluorescence (XRF) was conducted on a Rigaku Supermini200 instrument in a He atmosphere. Pt L_{III}-edge X-ray absorption spectroscopy (XAS) measurements were performed at the QAS beamline of the National Synchrotron Light Source II at Brookhaven National Laboratory in transmission mode. The surface stoichiometry measurements were performed using a Thermo Scientific K-Alpha X-ray photoelectron spectrometer (XPS) System. The XPS data were calibrated using the binding energy of adventitious carbon at 284.5 eV and analyzed using the CasaXPS software. All peaks were fitted using a Gaussian/Lorentzian product line shape and a Shirley background.

Catalytic Reactions

0.088 M 4-methyl-1-benzyl alcohol (4MBA, Sigma Aldrich), 100 mg catalyst, 20 ml anhydrous isopropanol (IPA, Sigma Aldrich), and a magnetic stirring bar were added to a Parr autoclave with a Teflon liner. The sealed reactor was flushed with nitrogen 5 times and charged with 100 psig H_2 and then N_2 to 260 psig at room temperature. The reactor was stirred and heated at 180 °C for 2 h. After the reaction, the liquid products were collected and diluted with IPA to 50 ml. Liquid products were filtered by a syringe filter and analyzed in an Agilent 7890B GC equipped with an HP-INNOWAX-19091N-133l column and a flame ionization detector. Products were identified using a SHIMADZU gas chromatograph-mass spectrometer (GCMS) QP2010 Plus system. Spent catalysts were washed by IPA, collected by vacuum filtration, and dried at 90 °C in an oven, named as $1Pt_1$-spent. They were further calcined in 200 ml/min air at 450 °C for 2 h at 10 °C/min to remove surface organics and then regenerated per the redispersion method mentioned above. The regenerated catalyst was named $1Pt_1$-spent-R.

Density-Functional Theory (DFT) Calculations

Spin-polarized periodic-DFT calculations were used to model Pt_n (n=1-4) on anatase TiO_2(101). The surface was represented by a four-layer (the bottom two layers were fixed) 1×3 slab separated by its periodic image in the z-direction by a vacuum region of 15 Å; the physical dimensions of the 1×3 slab were $10.43 \times 11.4 \times 28$ Å. The lattice parameters of the optimized bulk were a = b = 3.801 Å and c = 9.716 Å, similar to the values obtained in the literature using the same functional.[9, 36] We employed the Perdew-Burke-Ernzerhof (PBE)[37] theory level with dipole corrections. The projector-augmented wave (PAW)[38, 39] method was used to model the core electrons. Conventional valence configurations were employed for all elements except for Ti for which the semicore *p*-states and *s*-states were also included in the valence shell, respectively ("Ti_sv" in VASP). We used PAW_PBE 08Apr2002 for C, I, and, O, PAW_PBE 04Feb2005 for Pt, and PAW_PBE 26Sep2005 for Ti_sv. The +U method (U_{eff} = 3.5 eV on Ti *3d* states[40]) was applied to address the self-interaction problem. For all structures, an energy cutoff of 400 eV (600 eV for bulk) was used. The Brillouin zone was sampled on $(3 \times 3 \times 1)$ k-point grid. A Gaussian smearing of 0.1 eV width was used. The SCF iterations were converged to 10^{-6} eV and 10^{-4} eV for the bulk and slab calculations, respectively. Geometries were optimized to 0.01 eV/Å and 0.03 eV/Å for the bulk and slab calculations, respectively. A scaling factor[41] 1.0088 was applied to all frequencies to account for the difference from the experimental CO frequency (2143 cm^{-1}). Bader charge analysis[42] was performed using the Henkelman *et al.* implementation.[43] Binding energy of x (x = I, CO) was calculated via the following equation: $E_{b,X} = E_{x/TiO2} - E_{TiO2} - E_x$ where $E_{x/TiO2}$, E_{TiO2}, and E_x indicate electronic energies of the system with an adsorbate on TiO_2, the pristine TiO_2, and the isolated adsorbate in the unit cell, respectively. All DFT calculations were performed with the Vienna ab-initio simulation package (VASP, version 5.4.1[38, 44]).

3. Results and Discussion

Catalyst Redispersion

The IWI method afforded $1Pt_{NP}$ with a mean size of 1.6 nm as evidenced in AC-HAADF-STEM images (Figure 1a). The $2Pt_{NP}$ possessed a slightly larger mean size (1.7 nm, Figure S1a). No Pt diffraction patterns were observed in XRD, indicative of the small NPs (Figure S2). A representative HADDF-STEM image upon redispersion (Figure 1b) of a $1Pt_1$ sample clearly shows isolated Pt atoms and a small fraction of clusters (<1 nm), suggesting NPs were successfully redispersed. A small fraction of clusters and NPs are observed on the $2Pt_{NP}$ sample and the average size shrunk to <~1 nm (Figure S1b). XRF (Table S1) and inductively coupled plasma-optical emission spectrometry (ICP-OES, Table S2) indicate that the loading of Pt remains unchanged upon redispersion (negligible Pt loss).

FTIR spectra of CO adsorption corroborate the preceding observations. CO adsorption on Pt is well documented.[45] A significant fingerprint of CO adsorbed on isolated cationic Pt species ($Pt^{\delta+}$) is the symmetric sharp peak above 2110 cm^{-1}.[9, 23] On metallic Pt, the adsorption band ranges from 2034 to 2100 cm^{-1} with varying Pt coordination number.[46] The lower wavenumbers correspond to lower Pt coordination; CO adsorbed on (100) and (111) planes affords a wavenumber of 2084 and 2096 cm^{-1}, respectively.[46]

The $1Pt_{NP}$ samples before redispersion possess a broad CO adsorption band between 2070 and 2090 cm^{-1}, characteristic of metallic NPs (Figure 1c) and a peak at 2118 cm^{-1}, suggestive of a dispersed catalyst. After redispersion, the broadband disappears, and the CO adsorption peak shifts to 2118 cm^{-1}, corresponding to isolated or highly-dispersed $Pt^{\delta+}$ sites.[9] The $2Pt_{NP}$ sample exhibits a predominant peak at 2088 cm^{-1} representing NPs (Figure S1c).[9] This peak decreases to a tiny one upon redispersion, suggesting most NPs get redispersed, and a few small NPs or clusters remain. The major peak at 2118 cm^{-1}

characteristic of isolated $Pt^{\delta+}$ sites is in line with STEM images. The results demonstrate the effectiveness of the CH_3I/CO-assisted redispersion in reducing the size of the 1 wt% Pt NPs and its reduced efficiency for the 2 wt% sample.

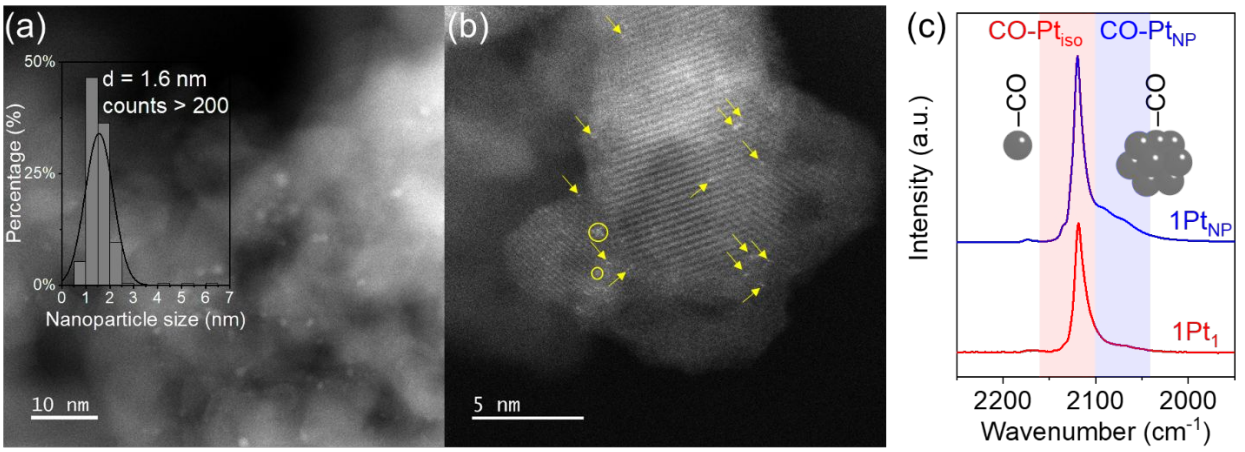

Figure 1. Characterization data before and after redispersion. AC-HAADF-STEM images of (a) $1Pt_{NP}$ and (b) $1Pt_1$. Yellow arrows mark isolated Pt atoms (Pt_{iso}) and circles mark clusters. (c) FTIR spectra of CO adsorption of $1Pt_{NP}$ and $1Pt_1$.

We then probed the local coordination of the $1Pt_{NP}$ catalysts by combining X-ray absorption spectroscopy (XAS) and X-ray photoelectron spectroscopy (XPS). As shown in the Pt L_{III}-edge k^2-weighted extended X-ray absorption fine structure (EXAFS) spectra (Figure 2a), $1Pt_{NP}$ has a significant peak at ~2.1 Å, ascribed to Pt-Pt coordination, according to the reference spectrum obtained from a Pt foil. This Pt-Pt coordination disappears in the $1Pt_1$ sample, suggesting successful redispersion of Pt NPs. Instead, a peak at ~ 1.6 Å is observed in $1Pt_1$, attributed to the coordination of Pt single atoms to neighboring oxygens in the TiO_2 support. The EXAFS spectra corroborate with complete redispersion.

X-ray absorption near edge structure (XANES) spectra suggested that $1Pt_{NP}$ has an almost identical white-line intensity as a Pt foil, suggesting a metallic state (Figure 2b). The $1Pt_1$ shows a white-line intensity between Pt^{4+} (PtO_2) and Pt^0 (Pt foil), suggesting oxidized Pt atoms upon redispersion, consistent with the Pt-O coordination. In line with the XANES results, Pt4*f* XPS data also suggests pure Pt^0 in the $1Pt_{NP}$ sample, and a shift of the Pt4*f* binding energy to higher values for the $1Pt_1$ sample (Figure 2c). Further peak deconvolution suggested Pt^{4+} is the major oxidation state in $1Pt_1$, with a small amount of metallic Pt^0.

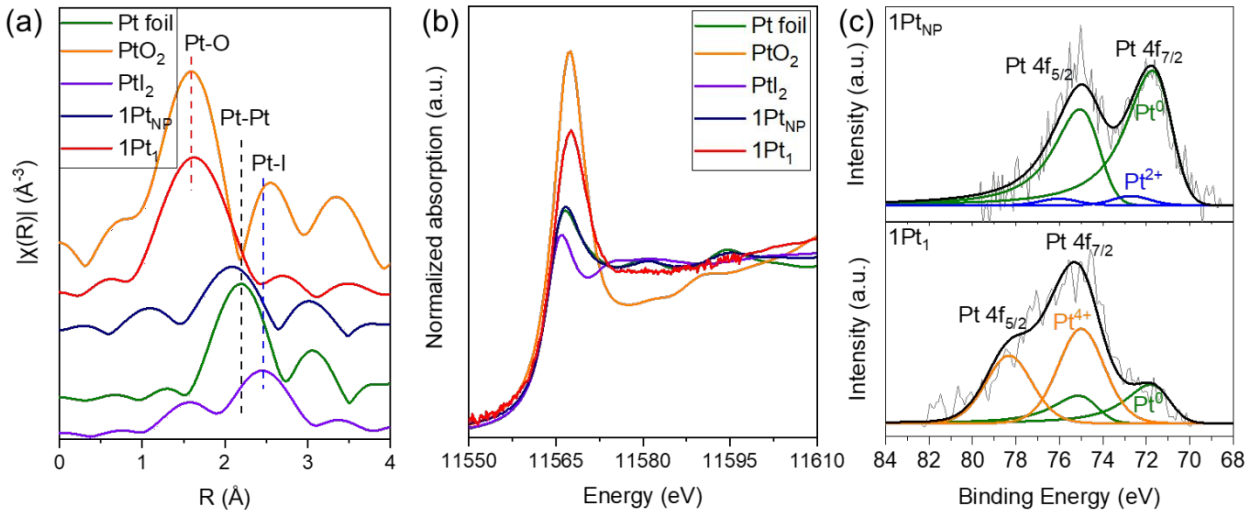

Figure 2. Effect of redispersion on coordination environment and oxidation state of the catalysts. Pt L_{III}-edge XAS and Pt*4f* XPS data of the $1Pt_{NP}$ catalysts. (a) Fourier-transformed k^2-weighted EXAFS spectra in R-space (without phase correction), (b) normalized XANES spectra, and (c) Pt*4f* XPS spectra.

XANES spectra of $2Pt_{NP}$ possess a slightly larger white-line intensity than the Pt foil (Figure S3a), probably due to its exposure to air before analysis, consistent with the deconvoluted Pt*4f* XPS spectra, where a small amount of Pt has an oxidation state of Pt^{4+} (Figure S3b). After redispersion, $2Pt_1$ shows a white-line intensity higher than $2Pt_{NP}$ and lower than Pt^{4+} (PtO_2), suggesting further oxidized Pt atoms. Peak deconvolution of the XPS data suggests Pt^{4+} is the major oxidation state in $2Pt_1$, mixed with Pt^{2+} and metallic Pt^0, consistent with the XANES data. We also observed a BE shift of Pt$4f_{7/2}$ species assigned to the Pt^0 from a higher value to a slightly lower value for NP samples ($1Pt_{NP}$ and $2Pt_{NP}$) to the redispersed samples ($1Pt_1$ and $2Pt_1$), and the trend was similar in the 1 wt% and 2 wt% samples, as shown in Figure 2c and Figure S3b. Ti*2p* XPS spectra were also analyzed and Ti^{4+} was the major component both before and after redispersion, with a very small fraction of Ti^{3+} species (Figure S4 and Table S3). The Pt/Ti atomic ratio was obtained from the core-level Pt and Ti spectra, with the relative sensitivity factors of 4.674 and 1.798, respectively. The Pt/Ti ratio increased after redispersion for both 1 wt% and 2 wt% samples, as shown in Table S3. The XAS and XPS results both suggest oxidation of Pt in the redispersion. It has been suggested[32] that iodine radicals attack and dissociate the Pt-Pt bonds, and Pt atoms get oxidized by the free iodine radicals. Pt atoms coordinate with the oxygen of TiO_2 and get stabilized. For the redispersion of Rh NPs on AC, the authors suggested that Rh-I and Rh-CO coordination also contributes to the stabilization of isolated Rh atoms in addition to the oxygen-containing groups on AC.[32] On the TiO_2 support, we did not observe Pt-I or Pt-CO coordination probably because TiO_2 has sufficient surface oxygen, compared to AC, to strongly interact with cationic Pt. Nevertheless, some iodine species and CO are still attached after redispersion, as evidenced by the *in-situ* mass spectra (MS) analysis shown in Figure S5a.

Thermal stability of redispersed catalysts

The thermal stability of SACs is a critical concern,[24, 47] especially at high metal loadings,[48] as they tend to sinter upon heating.[49, 50] One can combat this problem by lowing the metal loading, strengthening the metal-support interaction, or adding protective ligands.[51, 52] To assess this, we treated the redispersed Pt catalysts at 250 °C in Ar, and *in-situ* MS spectra were recorded (Figure S5a). Iodine-containing compounds (CH_3I or HI) desorbed at 224 °C, and CO desorption started at 231 °C and the desorption peak was at 258 °C.

DFT calculations (see next section) find stronger CO binding on Pt species ($E_{bind,CO}$=2.8-3.1 eV) compared to iodine-containing compounds on the support and Pt ($E_{bind,CH3}$ = 1.3 eV, $E_{bind,I}$ = 0.36 eV, $E_{Pt\text{-}(I)2\text{-}CO \rightarrow Pt\text{-}(I)\text{-}CO+I}$ = 0.9 eV), which suggest a higher CO desorption temperature than the iodine species.

The desorption of iodine and CO might cause re-sintering, and therefore, FTIR-CO was conducted again after thermal treatment. Neither Ar nor H_2/Ar post-treatment induced significant Pt agglomeration, as the major adsorption peak remains at 2118 cm^{-1} (Figure S5b). A tiny peak formed at ~2063 cm^{-1} that is lower than on Pt NPs (before redispersion; 2088 cm^{-1}, as shown in Figure S1c).[9] This might be assigned to CO adsorbed on clusters of low Pt-Pt coordination number of ~5.[46] The results indicate the redispersed $1Pt_1$ catalyst possesses thermal stability.

Theoretical investigation of the role of I● on CO vibrational frequencies and redistribution mechanism

To investigate the I● effect on the Pt_n structures and the corresponding CO vibrational frequencies, various Pt_n (n=1-4) structures[41, 53] were optimized on the anatase TiO_2(101) in the absence (

Figure **3**a-d) and presence (

Figure **3**e-h) of I● (dissociated from CH_3I[54]) via DFT. Different numbers of I● were introduced to Pt_1 to create Pt_1-$(I)_m$ (m=1-4). The introduction of two I● on the Pt_1-CO complex results in a stable 16 e^- square planar configuration[54, 55] (

Figure **3**e) with the strongest CO binding (Table S4), which was used for investigating the Pt_n-$(I)_2$ configurations. CO on the atop site was introduced on the most stable Pt_n configurations. We optimized various Pt_n-$(I)_2$ configurations with different starting geometries to obtain the most stable Pt_n-$(I)_2$ (

Figure **3**e-h). Pt_n as dopants (replacing surface Ti atoms) and Pt_n (n=1-4) as a combination of dopants and adatoms were also investigated. We observed no interaction between I● and doped Pt_n, as I● would only bind to Pt adatoms with a lower coordination number or form I_2 on the surface. Hence doped Pt configurations were not considered any further.

In the absence of I●, we observe a gradual decrease in the CO vibrational frequencies (from 2084 to 2025 cm^{-1}) with increasing Pt_n size (Figure 4). The CO vibrational frequency on Pt_1 is lower than the experimental values (>2110 cm^{-1}). Deprotonated hydroxyl groups on the support can provide comparable CO vibrational frequencies as suggested in the literature[55] (Figure 4, blue points). Irrespective of the absolute values, the shift in the CO vibrational frequencies vs. Pt_n size holds. Upon introducing I●, the most stable geometries and the CO vibrational frequencies fluctuate with Pt_n size. For $Pt_{(n=1\text{-}2)}$-$(I)_2$, the most stable configurations are similar to $Pt_{(n=1\text{-}2)}$ (

Figure **3**a-b and

Figure **3**e-f); the only differences are the Pt-I bonds and the Pt-O coordination location. On the other hand, a significant increase in vibrational frequencies is observed for the Pt_1-$(I)_2$-(CO) complex (2084 → 2110 cm^{-1}), rationalized by the rise in the partially positive Bader charge of Pt (0.12 →0.34 e^-) (Table S5). More importantly, the CO vibrational frequency of Pt_1-$(I)_2$-(CO) is now within the experimentally observed CO fingerprint of isolated cationic Pt species (> 2110 cm^{-1})[56, 57].

With increasing size, $Pt_{(n=1\rightarrow2)}$, a redshift in CO vibrational frequencies is seen as expected. However, a blueshift is observed for $Pt_{(n=2\rightarrow4)}$. This could be understood as the mononucleated Pt_1-$(I)_2$-(CO) complex, a 16 e^- square planar configuration, is preferred over the $Pt_{(n=3,4)}$-$(I)_2$. The promoting role of I● on forming mononucleated Pt_1 species is more evident on Pt_4 as the geometries differ significantly in the presence of I● (

Figure **3**d and

Figure **3**h). Specifically, the most stable Pt configuration is a pyramid and is favored over the planar geometry (found for $Pt_{\underline{4}}$-$(I)_2$) by 1.2 eV. In stark contrast, introducing I● renders the planar geometry favored over the pyramid by 1.1 eV. The planar geometry of $Pt_{\underline{4}}$-$(I)_2$ facilitates the dispersion of $Pt_{\underline{1}}$, as Pt is now readily oxidized upon introducing CO (the Bader charge of Pt with CO is 0.40 e^-), resulting in the blueshift in the CO vibrational frequency.

Based on these trends in $Pt_{\underline{n}}$ geometry and CO vibrational frequencies, we postulate that I● destabilizes the 3D Pt nanoparticles and cooperatively with CO form Pt_1 complexes on the support. The EXAFS data does not indicate any Pt-I or Pt-CO bonds (Figure 2a), which differs from the proposed Pt_1 configurations (

Figure **3**e). However, Pt_{NP} can readily oxidize to PtO_x upon exposure to air.[58] This may be occurring to our samples as Pt-I and Pt-CO could transform to Pt-O upon exposure to air for the EXAFS experiments. Replacement of Pt-I by Pt-O bond from the air could be preferred as the binding energies of the complexes Pt-$(O)_2$-CO and Pt-$(I)_2$-CO on the support (

Figure **3**a-d) imply the former is more stable by 1.5 eV. The displaced I, CH_3 radical and/or CO remain on the TiO_2 surface indicated by the favorable binding energy (E_{bind} is 0.36, 1.3 and 0.34 eV, respectively) consistent with the detection of CH_3I or HI and CO in MS data (Figure S5a).

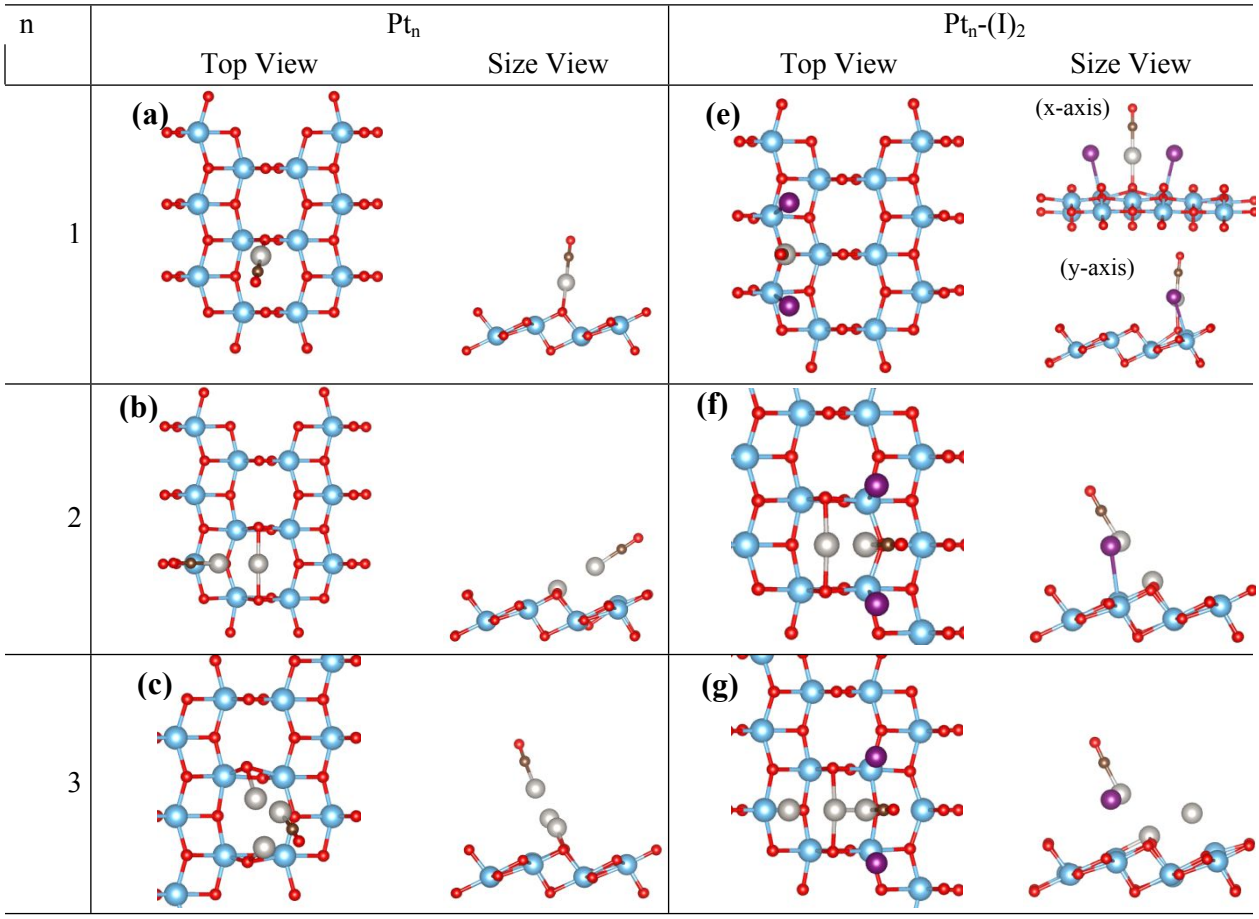

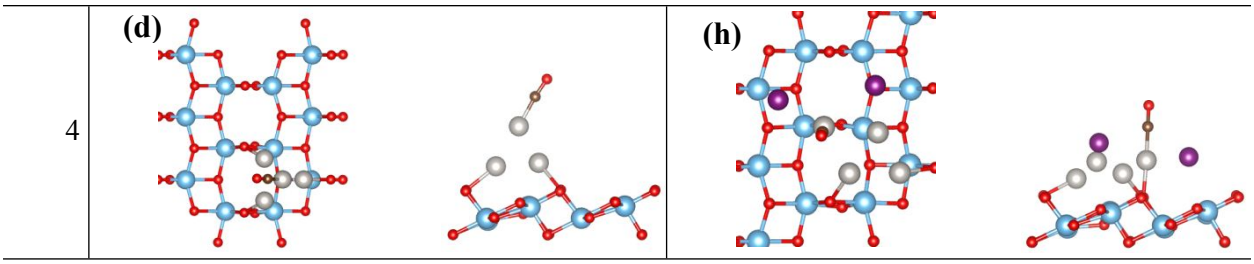

Figure 3. Most stable Pt_n (n=1-4) structures with CO adsorbed in the absence and presence of I●. Ti, O, C, Pt, and I are represented in blue, red, brown, silver, and purple, respectively. Only the top TiO_2 layer is shown. The corresponding CO vibrational frequencies are presented in Figure 4 and are summarized in Table S5.

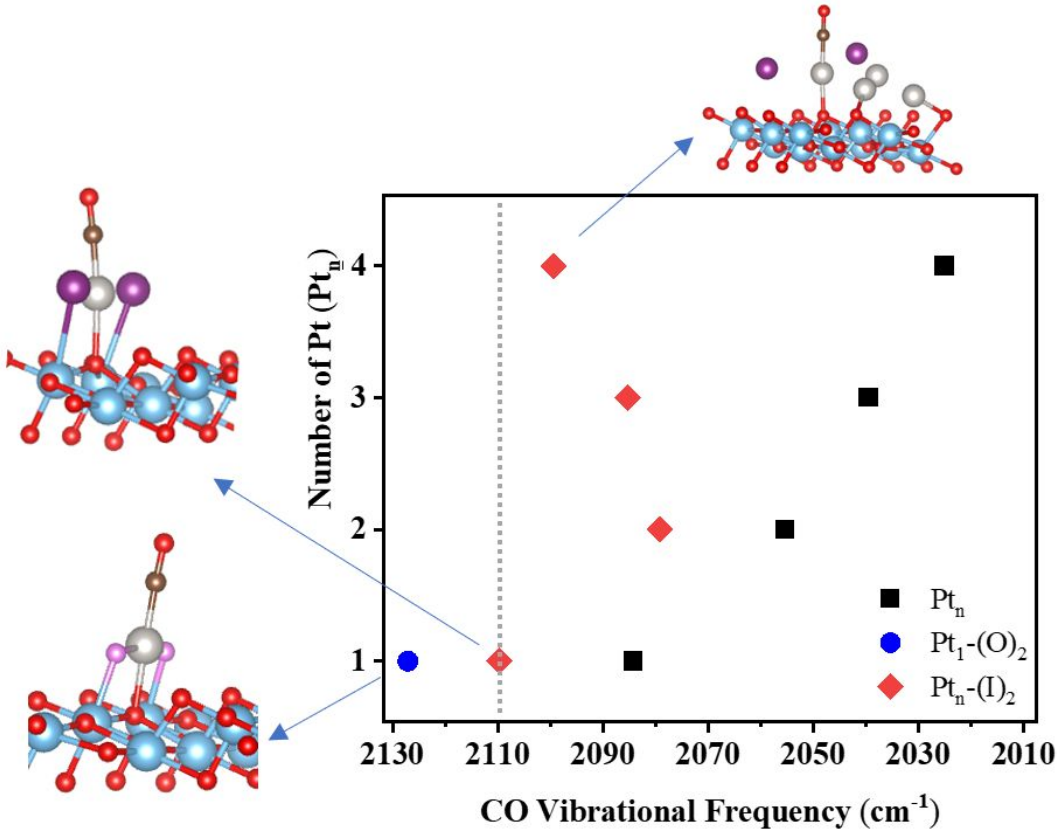

Figure 4. DFT-computed CO vibrational frequencies on Pt_n (n=1-4). Pt_n in the absence and presence of I● are shown in blue and red. Pt_1 under oxidative conditions is shown in blue. Gray dotted line (drawn at 2110 cm^{-1}) indicates the distinctive CO vibrational frequency of isolated cationic Pt species to the left of the line and metallic Pt to the right of it. Schematics surrounding the plot show three Pt configurations (top layer of TiO_2 is shown) with the highest CO vibrational frequencies. Ti, O (excess O), C, Pt, and I are represented in blue, red (prink), brown, silver, and purple, respectively.

Catalytic performance in HDO reaction

HDO of 4-methyl-1-benzyl alcohol (4MBA) to *p*-xylene was selected as a model reaction. 4MBA is a bio-oil-related building block containing a benzyl ring and a hydroxyl group, and the HDO of 4MBA produces *p*-xylene.[59, 60] Activating the C-O bond to form p-xylene (Figure 5a) is challenging.[61-63] The H_2

pressure and elevated temperatures naturally lead to side reactions, such as ring hydrogenation, etherification, and -CH_2OH dehydrogenation (Figure 5a).

TiO_2 has a minor activity, affording 5.1% conversion and only 1.3% selectivity to p-xylene (Figure 5b), due to the low density of surface oxygen vacancies. $1Pt_{NP}$ and $2Pt_{NP}$ catalysts significantly increase the 4MBA conversion but give a selectivity of 19% and 20% to ring saturated (RS) products, 5.9% and 1.4% to *p*-tolualdehyde (via dehydrogenation of 4MBA), and 2.9% and 6.9% to ether over surface acid sites, [64] respectively, i.e., these catalysts are not very selective.

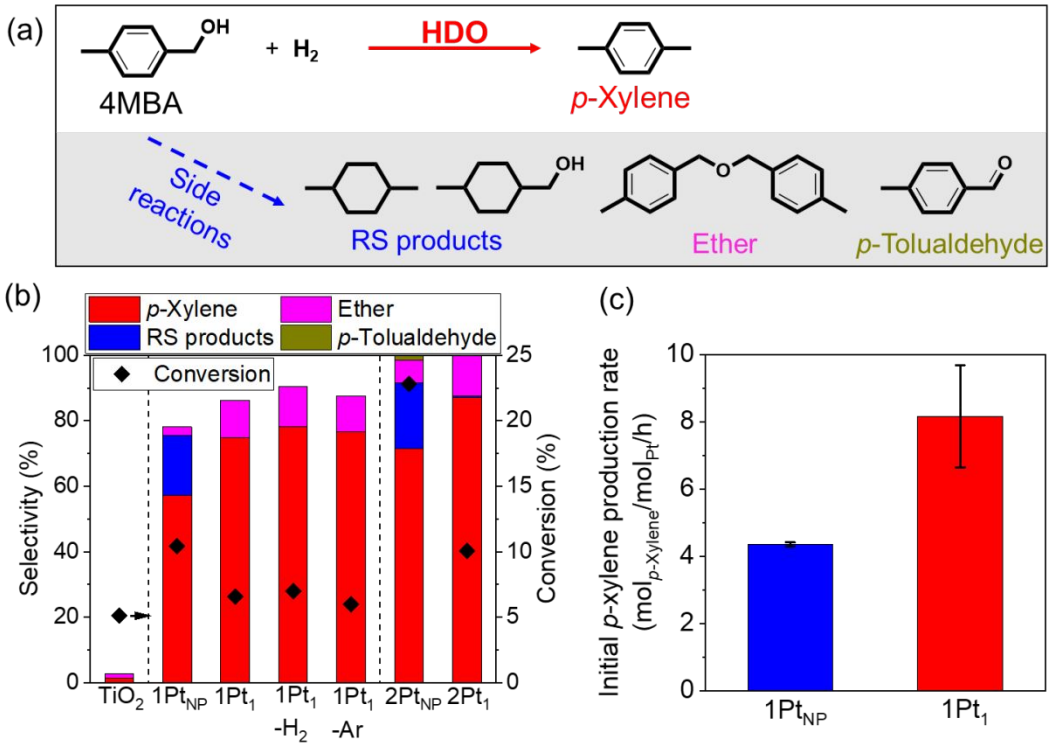

Figure 5. Catalytic performance comparison. (a) Schematic of HDO of 4MBA to *p*-xylene and possible side products, (b) catalytic performance of various Pt/TiO_2 catalysts for HDO of 4MBA for 2 h, and (c) initial reaction rates of $1Pt_1$ and $1Pt_{NP}$. Reaction conditions: 0.088 M 4MBA, 20 ml iso-propanol (IPA), 100 mg catalyst, 100 psi H_2 and 160 psi N_2 at room temperature, reaction at 180 °C.

After redispersion, the HDO selectivity to *p*-xylene over the $1Pt_1$ catalyst increases to 80% with no RS products, suggesting the side hydrogenation reactions are successfully inhibited. A noticeable increase in ether formation (13% selectivity) is likely caused by the iodine's stronger surface acidity. The etherification is a reversible reaction that can reverse to the main product with increasing time. The $1Pt_1$ catalyst gives 10x higher yield to p-xylene than a typical low loading, 0.04% Pt catalyst, used to prevent nanoparticles. The results indicate that the higher loading of Pt enhances vacancy formation and the rate. Similarly, the selectivity to *p*-xylene over $2Pt_1$ reaches 85%, with tiny RS products (0.3% selectivity). Upon flushing the catalyst by flowing Ar and H_2 at 250 °C (see Methods) to remove the residual iodine, the $1Pt_1$-H_2 and $1Pt_1$-Ar catalysts are comparable to the untreated catalyst (Figure 3b), suggesting no Pt agglomeration, consistent with the FTIR-CO results.

Kinetics measurements at low conversions (<10%, Figure S6) provided the initial HDO rates (Figure 5c). The initial *p*-xylene production rate was calculated from the slope of moles of *p*-xylene produced over the first hour of reaction and the moles of Pt loading obtained by ICP-OES (Table S2). The $1Pt_1$ almost

doubles the initial *p*-xylene production rate of $1Pt_{NP}$. This result stems from the complex interplay of (1) the different number of redox Pt sites on SACs compared to the peripheral sites of NPs and (2) the presence of metallic sites on Pt NPs that also perform HDO chemistry but with lower intrinsic activity than redox sites. For example, redox sites are 2.3 times more effective than metallic Pt sites for furan HDO chemistry.[9] The results suggested that the redispersed $1Pt_1$ catalyst provides enhanced selectivity to the desired product and intrinsic activity than Pt NPs with the same metal loading. The activity of $1Pt_1$ to the desired product is about 70 times higher than that of TiO_2 (Figure 5b). This indicates the profound effect of increasing the metal loading.

Next, we investigate the spent catalyst performance and regeneration. The $1Pt_1$-spent catalyst was washed by IPA and dried before being directly used in HDO reactions. It showed nearly half the conversion of the fresh $1Pt_1$, lower selectivity to *p*-xylene, and 26% selectivity to RS products (Figure S7a). The formation of RS products is a signature of sintering and is consistent with the FTIR-CO spectra (Figure S7b).

Upon regeneration of the $1Pt_1$-spent catalyst with the redispersion method, the catalyst ($1Pt_1$-spent-R) recovers its conversion (6.3%, Figure S7a). The selectivity to *p*-xylene increased slightly compared to the spent catalyst, and the selectivity to RS products was significantly inhibited to 2.6% (Figure S7a). According to the FTIR-CO spectra of the $1Pt_1$-spent-R, the peak for NPs substantially decreased and that of the single atoms recovered. The results suggested that the regeneration can redisperse the NPs formed during HDO reactions and recover its HDO activity but the selectivity only partially. It appears that the reaction causes multiple catalyst deactivations potentially through coke formation that retard the redox sites from doing the selective chemistry.

4. Conclusions

We presented a simple approach to prepare higher loadings of reducible metal oxide-supported Pt single atom and cluster catalysts through redispersion of Pt nanoparticles (NPs). CH_3I/CO treatment of Pt NPs on TiO_2 at mild temperature (240 °C) dispersed the catalyst as confirmed by CO FTIR, AC-HAADF-STEM, and XAS. The SACs remained stable after heat treatment in Ar or reduction in H_2/Ar at 250 °C, suggesting good thermal stability. DFT-computed IR frequencies corroborate with the experimental findings. The formation of Pt-$(I)_2$-CO complex results in a stable 16 e^- square planar configuration. Iodine makes the structures planar and with CO induce redispersion. Unlike carbon, neither Pt-I nor Pt-CO coordination is seen because TiO_2 has sufficient surface oxygen to anchor the redispersed Pt. DFT calculations support that Pt-$(O)_2$-CO is significantly more stable than Pt-$(I)_2$-CO. Using the HDO reaction of 4-methyl-1-benzyl alcohol as a showcase, we demonstrated that the ring hydrogenation was suppressed almost completely using dispersed SACs. Notably, the dispersed SACs afforded a higher initial *p*-xylene production rate than NPs with the same metal loading and a better selectivity and a remarkable ~70x increased activity compared to the bare support. The excellent selectivity to the desired product minimizes downstream separations. This approach might further be applied to more noble metals and metal oxides.

Acknowledgments

This work was supported and intellectually defined by the Catalysis Center for Energy Innovation, an Energy Frontier Research Center funded by the US Dept. of Energy, Office of Science, Office of Basic Energy Sciences under award number DE-SC0001004. The TEM work was performed in part at the Singh Center for Nanotechnology at the University of Pennsylvania, a member of the National Nanotechnology Coordinated Infrastructure (NNCI) network, which is supported by the National Science Foundation (Grant

NNCI-1542153). A. F. and E.A.S. gratefully acknowledge use of facilities and instrumentation supported by NSF through the University of Pennsylvania Materials Research Science and Engineering Center (MRSEC) (DMR-1720530); and the support for Integrated Mesoscale Architectures for Sustainable Catalysis (IMASC), an Energy Frontier Research Center funded by the U.S. Department of Energy, Office of Science, Basic Energy Sciences under Award #DE-SC0012573. This research used beamline 7-BM (QAS) of the National Synchrotron Light Source II, a U.S. Department of Energy (DOE) Office of Science User Facility operated for the DOE Office of Science by Brookhaven National Laboratory under Contract No. DE-SC0012704. QAS beamline operations were supported in part by the Synchrotron Catalysis Consortium (U.S. DOE, Office of Basic Energy Sciences, Grant No. DE-SC0012335).

References

1. A. V. Mironenko and D. G. Vlachos, *J. Am. Chem. Soc.* , 2016, **138**, 8104–8113.
2. W. Jin, L. Pastor-Pérez, D. Shen, A. Sepúlveda-Escribano, S. Gu and T. Ramirez Reina, *ChemCatChem*, 2019, **11**, 924-960.
3. Z. Lin, R. Chen, Z. Qu and J. G. Chen, *Green Chem.*, 2018, **20**, 2679-2696.
4. S. Kim, E. E. Kwon, Y. T. Kim, S. Jung, H. J. Kim, G. W. Huber and J. Lee, *Green Chemistry*, 2019, **21**, 3715-3743.
5. G. Liu, A. W. Robertson, M. M.-J. Li, W. C. H. Kuo, M. T. Darby, M. H. Muhieddine, Y.-C. Lin, K. Suenaga, M. Stamatakis, J. H. Warner and S. C. E. Tsang, *Nat. Chem.*, 2017, **9**, 810–816.
6. X. Wang, P. Wu, Z. Wang, L. Zhou, Y. Liu, H. Cheng, M. Arai, C. Zhang and F. Zhao, *ACS Sustainable Chem. Eng.*, 2021, **9**, 3083-3094.
7. J. Luo, M. Monai, H. Yun, L. Arroyo-Ramírez, C. Wang, C. B. Murray, P. Fornasiero and R. J. Gorte, *Catal. Lett.*, 2016, **146**, 711–717.
8. K. A. Goulas, A. V. Mironenko, G. R. Jenness, T. Mazal and D. G. Vlachos, *Nat. Catal.*, 2019, **2**, 269-276.
9. J. Fu, J. Lym, W. Zheng, K. Alexopoulos, A. V. Mironenko, N. Li, J. A. Boscoboinik, D. Su, R. T. Weber and D. G. Vlachos, *Nat. Catal.*, 2020, **3**, 446–453.
10. E. Iglesia and M. Boudart, *J. Phys. Chem.*, 1991, **95**, 7011–7016.
11. Z. Li, S. Ji, Y. Liu, X. Cao, S. Tian, Y. Chen, Z. Niu and Y. Li, *Chemical reviews*, 2020, **120**, 623-682.
12. L. Liu and A. Corma, *Chem Rev*, 2018, **118**, 4981-5079.
13. A. Beniya and S. Higashi, *Nature Catalysis*, 2019, **2**, 590-602.
14. X. Li, X. Yang, Y. Huang, T. Zhang and B. Liu, *Adv. Mat.*, 2019, **31**, 1902031.
15. B. Singh, V. Sharma, R. P. Gaikwad, P. Fornasiero, R. Zbořil and M. B. Gawande, *Small*, 2021, **17**, 2006473.
16. M. B. Gawande, K. Ariga and Y. Yamauchi, *Small*, 2021, **17**, 2101584.
17. S. Ji, Y. Chen, X. Wang, Z. Zhang, D. Wang and Y. Li, *Chemical reviews*, 2020, DOI: 10.1021/acs.chemrev.9b00818.
18. L. Zhang, M. N. Banis and X. Sun, *National Science Review*, 2018, **5**, 628–630.
19. J. Jones, H. Xiong, A. T. DeLaRiva, E. J. Peterson, H. Pham, S. R. Challa, G. Qi, S. Oh, M. H. Wiebenga, X. I. P. Hernández, Y. Wang and A. K. Datye, *Science*, 2016, **353**, 150-154.
20. K. Wang, X. Wang and X. Liang, *ChemCatChem*, 2021, **13**, 28-58.
21. B. Qiao, A. Wang, X. Yang, L. F. Allard, Z. Jiang, Y. Cui, J. Liu, J. Li and T. Zhang, *Nat. Chem.*, 2011, **3**, 634–641.
22. J. C. Matsubu, V. N. Yang and P. Christopher, *J. Am. Chem. Soc.*, 2015, **137**, 3076-3084.
23. L. DeRita, S. Dai, K. Lopez-Zepeda, N. Pham, G. W. Graham, X. Pan and P. Christopher, *J. Am. Chem. Soc.*, 2017, **139**, 14150-14165.
24. J.-C. Liu, Y. Tang, Yang-GangWang, T. Zhang and J. Li, *Natl. Sci. Rev.*, 2018, **5**, 638-641.

25. K. Morgan, A. Goguet and C. Hardacre, *ACS Catal.*, 2015, **5**, 3430-3445.
26. D. Kunwar, S. Zhou, A. DeLaRiva, E. J. Peterson, H. Xiong, X. I. Pereira-Hernández, S. C. Purdy, R. ter Veen, H. H. Brongersma, J. T. Miller, H. Hashiguchi, L. Kovarik, S. Lin, H. Guo, Y. Wang and A. K. Datye, *ACS Catal.*, 2019, **9**, 3978-3990.
27. R. Lang, W. Xi, J. C. Liu, Y. T. Cui, T. Li, A. F. Lee, F. Chen, Y. Chen, L. Li, L. Li, J. Lin, S. Miao, X. Liu, A. Q. Wang, X. Wang, J. Luo, B. Qiao, J. Li and T. Zhang, *Nature communications*, 2019, **10**, 234.
28. Y. Qu, B. Chen, Z. Li, X. Duan, L. Wang, Y. Lin, T. Yuan, F. Zhou, Y. Hu, Z. Yang, C. Zhao, J. Wang, C. Zhao, Y. Hu, G. Wu, Q. Zhang, Q. Xu, B. Liu, P. Gao, R. You, W. Huang, L. Zheng, L. Gu, Y. Wu and Y. Li, *J. Am. Chem. Soc.*, 2019, **141**, 4505-4509.
29. A. Goguet, C. Hardacre, I. Harvey, K. Narasimharao, Y. Saih and J. Sa, *J. Am. Chem. Soc.*, 2009, **131**, 6973-6975.
30. J. Sá, A. Goguet, S. F. R. Taylor, R. Tiruvalam, C. J. Kiely, M. Nachtegaal, G. J. Hutchings and C. Hardacre, *Angewandte Chemie*, 2011, **50**, 8912-8916.
31. K. Morgan, R. Burch, M. Daous, J. J. Delgado, A. Goguet, C. Hardacre, L. A. Petrov and D. W. Rooney, *Catal. Sci. Technol.*, 2014, **4**, 729.
32. S. Feng, X. Song, Y. Liu, X. Lin, L. Yan, S. Liu, W. Dong, X. Yang, Z. Jiang and Y. Ding, *Nature communications*, 2019, **10**, 5281.
33. S. Feng, P. Hemberger, A. Bodi, X. Song, T. Yu, Z. Jiang, Y. Liu and Y. Ding, *J. Catal.*, 2020, **382**, 347-357.
34. S. Feng, X. Lin, X. Song, B. Mei, J. Mu, J. Li, Y. Liu, Z. Jiang and Y. Ding, *ACS Catal.*, 2020, **11**, 682-690.
35. J. Sá, S. F. R. Taylor, H. Daly, A. Goguet, R. Tiruvalam, Q. He, C. J. Kiely, G. J. Hutchings and C. Hardacre, *ACS Catal.*, 2012, **2**, 552-560.
36. M. M. Islam, M. Calatayud and G. Pacchioni, *J. Phys. Chem. C*, 2011, **115**, 6809–6814.
37. J. P. Perdew, K. Burke and M. Ernzerhof, *Physical Review Letters*, 1997, **78**, 1396-1396.
38. G. Kresse and J. Furthmüller, *Computational Materials Science*, 1996, **6**, 15-50.
39. P. E. Blöchl, *Physical Review B*, 1994, **50**, 17953-17979.
40. H. Cheng and A. Selloni, *The Journal of Chemical Physics*, 2009, **131**, 054703.
41. H. V. Thang, G. Pacchioni, L. DeRita and P. Christopher, *Journal of Catalysis*, 2018, **367**, 104-114.
42. R. F. W. Bader, *Chemical Reviews*, 1991, **91**, 893-928.
43. G. Henkelman, A. Arnaldsson and H. Jónsson, *Computational Materials Science*, 2006, **36**, 354-360.
44. G. Kresse and J. Furthmüller, *Physical Review B*, 1996, **54**, 11169-11186.
45. C. Lamberti, A. Zecchina, E. Groppo and S. Bordiga, *Chem. Soc. Rev.*, 2010, **39**, 4951-5001.
46. M. J. Kappers and J. H. v. d. Maas, *Catalysis Letters*, 1991, **10**, 365-374.
47. H. Y. Zhuo, X. Zhang, J. X. Liang, Q. Yu, H. Xiao and J. Li, *Chemical reviews*, 2020, **120**, 12315-12341.
48. H. Jeong, S. Shin and H. Lee, *ACS Nano*, 2020, **14**, 14355-14374.
49. L. Li, X. Chang, X. Lin, Z. J. Zhao and J. Gong, *Chem. Soc. Rev.*, 2020, **49**, 8156-8178.
50. S. K. Kaiser, Z. Chen, D. Faust Akl, S. Mitchell and J. Perez-Ramirez, *Chemical reviews*, 2020, **120**, 11703-11809.
51. R. Lang, X. Du, Y. Huang, X. Jiang, Q. Zhang, Y. Guo, K. Liu, B. Qiao, A. Wang and T. Zhang, *Chemical reviews*, 2020, **120**, 11986-12043.
52. S. Ding, Y. Guo, M. J.Hülsey, BinZhang, H. Asakura, L. Liu, Y. Han, M. Gao, J.-y. Hasegawa, B. Qiao, T. Zhang and NingYan, *Chem*, 2019, **5**, 3207-3219.
53. Y. Han, C.-j. Liu and Q. Ge, *The Journal of Physical Chemistry B*, 2006, **110**, 7463-7472.
54. S. Feng, X. Song, Y. Liu, X. Lin, L. Yan, S. Liu, W. Dong, X. Yang, Z. Jiang and Y. Ding, *Nature Communications*, 2019, **10**, 5281.
55. C. A. Tolman, *Chemical Society Reviews*, 1972, **1**, 337-353.

56. J. Fu, J. Lym, W. Zheng, K. Alexopoulos, A. V. Mironenko, N. Li, J. A. Boscoboinik, D. Su, R. T. Weber and D. G. Vlachos, *Nature Catalysis*, 2020, **3**, 446-453.
57. L. DeRita, S. Dai, K. Lopez-Zepeda, N. Pham, G. W. Graham, X. Pan and P. Christopher, *Journal of the American Chemical Society*, 2017, **139**, 14150-14165.
58. L. K. Ono, J. R. Croy, H. Heinrich and B. Roldan Cuenya, *The Journal of Physical Chemistry C*, 2011, **115**, 16856-16866.
59. C. González, P. Marín, F. V. Díez and S. Ordóñez, *Ind. Eng. Chem. Res.*, 2016, **55**, 2319-2327.
60. L. Pan, Y. He, M. Niu, Y. Dan and W. Li, *J. Mater. Sci.*, 2019, **55**, 1614-1626.
61. L. Offner-Marko, A. Bordet, G. Moos, S. Tricard, S. Rengshausen, B. Chaudret, K. L. Luska and W. Leitner, *Angewandte Chemie*, 2018, **57**, 12721-12726.
62. J. Zhang, L. D. Ellis, B. Wang, M. J. Dzara, C. Sievers, S. Pylypenko, E. Nikolla and J. W. Medlin, *Nat. Catal.*, 2018, **1**, 148-155.
63. C. Mondelli, G. Gozaydin, N. Yan and J. Perez-Ramirez, *Chem. Soc. Rev.*, 2020, **49**, 3764-3782.
64. P. Lanzafame, K. Barbera, S. Perathoner, G. Centi, A. Aloise, M. Migliori, A. Macario, J. B. Nagy and G. Giordano, *J. Catal.*, 2015, **330**, 558-568.